Development of a Transient Kinetic Model for the Simultaneous Adsorption of SO 2 −NO x over Na/γ-Al 2 O 3 Sorbent

ARTICLE *in* INDUSTRIAL & ENGINEERING CHEMISTRY RESEARCH · JANUARY 2001

Impact Factor: 2.59 · DOI: 10.1021/ie000532o

4 AUTHORS:

Juray De Wilde
Université catholique de Louvain
67 PUBLICATIONS **520** CITATIONS
SEE PROFILE

Asit Kumar Das
Reliance Industries Limited
88 PUBLICATIONS **193** CITATIONS
SEE PROFILE

Geraldine J. Heynderickx
Ghent University
94 PUBLICATIONS **974** CITATIONS
SEE PROFILE

Bryan Marin
Ghent University
401 PUBLICATIONS **4,818** CITATIONS
SEE PROFILE

Article

Development of a Transient Kinetic Model for the Simultaneous Adsorption of SO–NO over Na/-AlO Sorbent

Juray De Wilde, Asit K. Das, Geraldine H. Heynderickx, and Guy B. Marin

Ind. Eng. Chem. Res., **2001**, 40 (1), 119-130 • DOI: 10.1021/ie000532o

Development of a Transient Kinetic Model for the Simultaneous Adsorption of SO_2-NO_x over $Na/\gamma\text{-}Al_2O_3$ Sorbent

Juray De Wilde, Asit K. Das, Geraldine H. Heynderickx, and Guy B. Marin*

Laboratorium voor Petrochemische Techniek, Universiteit Gent, Krijgslaan 281, S5, B-9000 Gent, Belgium

A transient kinetic model has been developed for the simultaneous adsorption of SO_2-NO_x on $Na/\gamma\text{-}Al_2O_3$ sorbent, using step response experimental data from a fixed-bed microreactor. The reactor temperature ranges from 367 to 407 K, and the molar SO_2/NO ratio from 2 to 8 with and without NO_2. SO_2 and NO_2 readily adsorb on the sorbent surface, producing SO_2* and NO_2* species. However, NO and O_2 only adsorb simultaneously and in the presence of sufficient SO_2* on the surface. The proposed mechanism consists of chemisorption steps for SO_2 and NO_2, whereas NO and O_2 are adsorbed simultaneously via an Eley−Rideal step involving a surface species derived from SO_2*. The latter is followed by several consecutive steps involving more SO_2* species as well as O_2, leading to the formation of a complex with a stoichiometry of $SO_2/O_2/NO$ of 10/5.5/1. The enhanced SO_2 sorption capacity in the presence of NO_2 is described adequately by considering that the adsorbed NO_2* opens a new reaction path for SO_2 adsorption. Both the Langmuir ideal surface and the Elovich nonuniform surface kinetics were considered for the steps involving free sites. The latter were found to simulate the experimental data more closely, indicating that the interaction among various species and intrinsic surface nonuniformity are important.

1. Introduction

SO_2 and NO_x (NO and NO_2) are the most commonly encountered air pollutants causing acid rain and are highly toxic to the environment and living species. These pollutants are emitted into the atmosphere mainly through automobile exhaust gases and the gases from oil/coal-fired furnaces, boilers, and refinery FCC units.

For cleaning of the industrial flue gases, only a few technology options are available, and they are often multistep, complex, and costly. For example, in many installations, the wet processes of Belco Tech. and Exxon, based on alkaline scrubbing of the flue gas, are in operation. Another wet process based on the catalytic conversion of SO_2 to SO_3 and subsequent condensation to sulfuric acid has been commercialized by Haldor Topsoe a/s (*Hydrocarbon Processing*, 1998). These processes can remove only SO_2 and often yield byproducts that are sometimes difficult to dispose. Moreover, for removal of the NO_x, the above-treated flue gas is further processed through selective catalytic reduction (SCR) of the NO_x with ammonia or other reducing agents to form nitrogen/water (Cho, 1994). The SCR process, as such, involves toxic gases and is very costly.

In light of the above, it is highly desirable to have a suitable single-step dry process for the removal of SO_2 and NO_x from the industrial flue gases. M/s FLS miljo a/s Denmark, has recently developed a new process (called SNAP) based on the simultaneous adsorption of SO_2 and NO_x on $Na/\gamma\text{-}Al_2O_3$ in a circulating dilute-phase riser reactor. This new process is dry and compact and has a high removal efficiency of SO_2 and NO_x (Mortensen, 1995). The process has been derived from the NOXSO process, which used larger sorbent particles in a dense-phase fluidized bed reactor (Ma et al., 1995).

The adsorption characteristics of SO_2 over $\gamma\text{-}Al_2O_3$ and sodium-impregnated $\gamma\text{-}Al_2O_3$ have been reported previously in the literature (Deo and Dalla, 1971; Karge and Dalla, 1984; Saad et al., 1993). However, the simultaneous adsorption of SO_2 and NO_x in a short-contact-time riser reactor (SNAP process) is a relatively new subject of study. To develop this process into a commercially viable technology, concerted efforts were made to understand the reaction mechanism and the kinetics of the simultaneous SO_2-NO_x adsorption on $Na/\gamma\text{-}Al_2O_3$. Recently, De Wilde and Marin (2000) reported experimental results of the above simultaneous adsorption. Their experiments were based on the introduction of stepwise changes in the composition of a gas mixture containing NO, O_2, NO_2, and SO_2 and continuously fed to a fixed-bed microreactor. The responses to these changes were monitored as a function of time. In the present study, a transient kinetic model is developed for the simultaneous SO_2-NO_x adsorption over $Na/\gamma\text{-}Al_2O_3$ sorbent using the above experimental data of De Wilde and Marin (2000). The kinetic model explains the complex interactions among the different components in the gas mixture and allows for a quantitative description of the experimental observations. Hence, it can be applied to simulate, design, and optimize processes such as SNAP.

2. Experimental Section

Figure 1 shows a schematic representation of the experimental setup. Table 1 summarizes the range of experimental conditions and the properties of the sorbent used in this study. As seen in Figure 1, two completely separated gas streams are available: an inert gas (argon) and the reaction mixture containing SO_2, NO, NO_2, O_2, and Ar. Both of the gas streams are preheated to 353 K before they are sent to the four-way valve in the oven/reactor section. To achieve a proper step input without fluctuation, it is essential to maintain

* Corresponding author. Phone: 32-9-2644516. Fax: 32-9-2644999. E-mail: guy.marin@rug.ac.be.

10.1021/ie000532o CCC: $20.00
Published on Web 11/18/2000

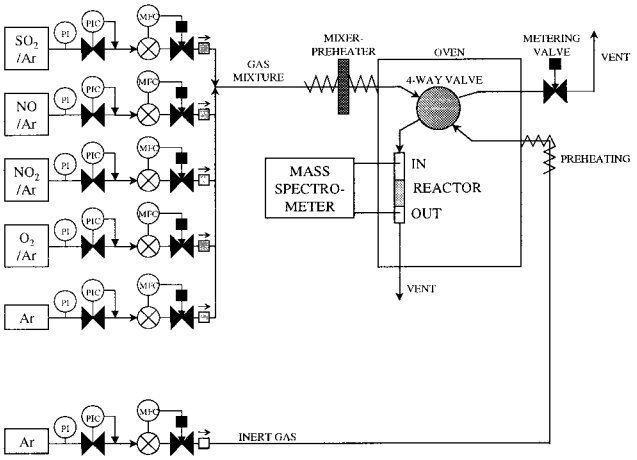

Figure 1. Schematic diagram of the experimental setup.

Table 1. Experimental Conditions and Sorbent Properties

parameter		value
reactor diameter, d_r	10^{-3} m	3.0
sorbent properties		
pore volume	10^{-3} m^3/kg	0.4
BET surface area	10^3 m^2/kg	227
pellet density, ρ_s	10^3 kg/m^3	1.55
pore diameter, $2r_o$	10^{-9} m	10
sorbent pellet diameter, d_p	10^{-6} m	250
pellet porosity, ϵ_p	−	0.5
amount of sorbent	10^{-3} kg	0.04
sorbent bed height, L	10^{-3} m	12
bed porosity, ϵ_b	−	0.5
temperature, T	K	367−407
gas flow rate	10^{-4} mol/s	2.088
concentration, C_i	mol %	
SO_2		0.86−2.3
NO		0.29−2.0
NO_2		0.0−0.43
O_2		0.0−1.5

equal flow rates and pressurs at both outlets of the four-way valve for the inert gas and the reacting gas. It is important to note that a significant quantity of water is usually present in industrial flue gases. The presence of water generally improves the sorbent capacity for SO_2 and NO_x adsorption. However, in the present work, all experiments were performed without feeding water in the inlet to avoid corrosion problems in the setup.

A fixed-bed plug-flow reactor is used for the experiments, which allows us to focus on the reaction mechanism at well-defined flow conditions. The reactor is made of borosilicate glass to avoid any corrosion by the reactive gas mixture. The length of the sorbent bed, the reactor diameter, the gas flow rate, and the pellet diameter are chosen so as to (i) maintain plug-flow conditions, (ii) ensure that the adsorption rate is not controlled by external diffusion, and (iii) limit the bed pressure drop to within 0.1 bar.

A Balzers ThermoStar quadrupole mass spectrometer (Pfeiffer Vacuum D35614 Asslar) is used for the measurement of the concentration of various components in transient mode. It is capable of providing analysis at a frequency of 30 s^{-1} with a gas mixture having four components.

The sorbent Na/γ-Al_2O_3 was provided as a powder with a mean particle size of 64 $\times$ 10^{-6} m. To avoid a high pressure drop over the sorbent bed, this powder is first pelletized and then crushed and sieved to obtain particles in the size range of (200−250) $\times$ 10^{-6} m, which is still small enough to avoid internal diffusion limitations. The sorbent is then dried for 5 h at 383 K and calcined for 15 h at 873 K. For each experiment, the reactor was loaded with a fresh batch of externally calcined sorbent so that, at $t = 0$, the sorbent was presumed to have only free sites. The sorbent properties are summarized in Table 1.

3. Modeling

To develop the appropriate reaction mechanism, it is necessary to first simulate the microreactor performance. The approach aims at calculating the reactor outlet concentrations of NO, O_2, NO_2, and SO_2 using the measured inlet concentrations of these components as boundary conditions and then estimating the kinetic parameters of the proposed model using nonlinear multiple-response regression analysis. To be able to use a pseudo homogeneous plug-flow model, it is necessary to verify the criteria for the plug flow and also to examine whether the effect of the external and internal diffusion on the kinetics of adsorption can be neglected.

Conventional criteria for ideal plug flow are

$$d_r/d_p > 10, \quad L/d_p > 50 \quad \text{and} \quad \mathrm{Re} = (\rho u_s d_p)/\mu > 10$$

For the experimental conditions employed in the present work, viz. Table 1, it follows that $d_r/d_p = 12$ and $L/d_p = 48$. Also, a typical Reynolds number in the present study is about 10 at the gas flow rate of 2.088 $\times$ 10^{-4} mol/s. Hence, plug flow can be assumed.

For transient experiments, Dekker et al. (1995) proposed a set of conditions to verify the influence of internal and external diffusion on the kinetic rate, which are as follows for spherical particles:

for negligible external resistance, $\mathrm{Bi}_m > 20$

for negligible internal resistance, with $\mathrm{Bi}_m > 20$,

$$\tau_{in} = [(D_e/\epsilon_p r^2)t] \geq 0.25$$

In the present study, because the majority of the gas mixture is argon, we have evaluated the above transient criteria for the argon system. As seen from Table 1, the average pore diameter ($2r_o$) of the sorbent used in this study is 10 nm, for which a value of 6.0 $\times$ 10^{-08} m^2/s (Andrieu and Smith, 1981) can be assumed for D_e. The molecular diffusivity D_m at 400 K is about 3.32 $\times$ 10^{-4} m^2/s, and the Schmidt number Sc = 0.0704. The Sherwood number is calculated from the correlation proposed by Chihara et al. (1978): $\mathrm{Sh} = (k_g d_p/D_m) = 2 + (1.1)(\mathrm{Sc})^{1/3}(\mathrm{Re})^{0.6}$. For Sc of 0.0704 and Re of 10.11, the Sherwood number amounts to 3.82, which corresponds to a mass transfer coefficient k_g of 5.05 m/s and a Biot number, $\mathrm{Bi}_m = k_g r/D_e$, of 1.05 $\times$ 10^4 for a 250-μm pellet diameter. Because Bi_m is much higher than 20, by applying the first criterion of Dekker et al. (1995), the external transport resistance can be assumed to be negligible.

From the second criterion, the minimum time necessary for negligible internal pore resistance amounts to 0.029 s for 10-nm pores, as compared to a typical experimental time scale of 25−30 s in this study. Hence, it is justified to neglect the internal mass transport resistance also.

In a similar manner, the effects of the extraparticle and intraparticle heat transport on the kinetics were

also found to be negligible, based on the criteria given by Dekker et al. (1995).

In addition to these above simplifications, the total molar flow rate can be assumed constant throughout the sorbent bed, as the reactive gas mixture is highly diluted with the inert gas argon. Furthermore, the sorbent bed temperature was measured to be constant during a typical adsorption experiment.

Model Equations. The model consists of the continuity equations for NO, O_2, NO_2, and SO_2 in the gas phase and of the surface species adsorbed on the sorbent. For a pseudo homogeneous ideal plug-flow model, the continuity equations for the gas-phase components are as follows:

$$\frac{\partial C_i}{\partial t} + \frac{u_s}{\epsilon}\frac{\partial C_i}{\partial z} = \frac{\rho_s}{\epsilon}(1 - \epsilon_b)C_t R_i \tag{1}$$

The continuity equations for the surface species j are written as follows:

$$\frac{\partial \theta_j}{\partial t} = R_j \tag{2}$$

The production rates in eqs 1 and 2 are calculated from the elementary reaction steps considered in the reaction mechanism

$$R_i = \sum_p \gamma_{i,p} r_{i,p} \tag{3}$$

where $\gamma_{i,p}$ is the stoichiometric coefficient of the component i in reaction step p and $r_{i,p}$ is the reaction rate of the elementary step p.

The initial and boundary conditions for eq 1 are given as

$$\text{at } t = 0, \quad z \geq 0, C_i = 0$$

$$\text{at } z = 0, \quad t > 0, C_i = C_i°(t) \tag{4}$$

The initial condition for eq 2 is given as

$$\text{at } z \geq 0, \quad t = 0, \theta_j = 0 \tag{5}$$

Numerical Calculations. The set of partial differential equations (PDEs), eq 1, for the gas-phase components and the set of ordinary differential equations (ODEs), eq 2, for the surface species were solved numerically. The PDEs were solved by employing the method of lines (Schiesser, 1991), which is a relatively simple numerical technique for converting PDEs into a system of ODEs. This is done by approximating all of the partial derivatives except one, usually the derivative with respect to time. One commonly practiced method for approximating the space derivatives is by finite differences. The resulting system of ODEs is then integrated simultaneously with a numerical ODE solver. More details on the finite difference approximations are available elsewhere (van der Linde et al., 1997). The Numerical Algorithm Group (NAG) subroutines used for the finite difference approximations are DO2NVF and DO2NTF, which achieve discretization by backward or upstream differentiation (NAG, 1991). The time integration was carried out using a backward differential formulation (BDF) integrator by using NAG subroutine DO2NCF. The program was implemented on a Solaris 2.4 Sun SPARC system and took about 30 s for simulation of one experiment and typically about 15 min for complete convergence during regression.

Regression Analysis. Estimation of the kinetic parameters was performed using nonlinear regression analysis of the outlet concentrations of all of the reactive components in the gas phase, namely, NO, O_2, NO_2, and SO_2. Parameter estimates were obtained by minimizing the objective function

$$S = \sum_{i=1}^{v}\sum_{k=1}^{n}[(y_{k,i} - \hat{y}_{k,i})]^2 \tag{6}$$

Because in the present work, the responses, i.e., the outlet concentrations of different gas-phase components, are of similar magnitude, weight factors are not considered in eq 6.

The multi-response Levenberg−Marquardt algorithm was adopted (Himmelblau, 1972). In the present work, there are four responses and seven observations covering a temperature range of 367−407 K. For each response, the experimental data were collected at time intervals of 0.4 s over a period of 25−30 s from the introduction of the step response, beyond which no appreciable change in the responses was noticed. Therefore, there are about 60 data points for each component in one observation and, all together, about 1680 data points for the global regression.

The statistical significance of the global regression is examined through the commonly used F test, which is based on the comparison of the sum of squares of the calculated response values and the residual sum of squares. A high value of F corresponds to a high significance of the regression. Usually, the statistical significance of the individual parameter estimates are tested based on their t values. In this case, it was observed that the calculated t values were rather high and in a range of 10^1−10^3 previously reported by Nibbelke et al. (1998). These values were also observed to be strongly dependent on the step size used for calculating the Jacobian matrix with respect to the parameters. Hence, instead of using t values, the model sensitivity of the model calculation on the values of the individual parameters was verified directly. Further, the possibility of local minimum was verified by providing different initial guesses for the parameters and observing whether they converged to the global solution or not.

The rate coefficients for the reactions are described in the following form:

$$k_i = k_{i,o}\exp\left[\frac{-E_i}{R}\left(\frac{1}{T} - \frac{1}{T_{av}}\right)\right] \tag{7}$$

Using the above form of the rate coefficients, the maximum binary correlation coefficient amounted to 0.71.

4. Reaction Mechanism

The data for a typical experiment at a SO_2/NO ratio of 8 and without NO_2 are presented in Figure 2. The SO_2 concentration at the reactor inlet increases to a set value of 2.2 mol % within 2 s. The breakthrough of SO_2 occurs about 8−10 s after introducing the step. After about 20 s, the SO_2 concentration at the outlet approaches the inlet concentration, indicating that free sites are no longer available for further adsorption.

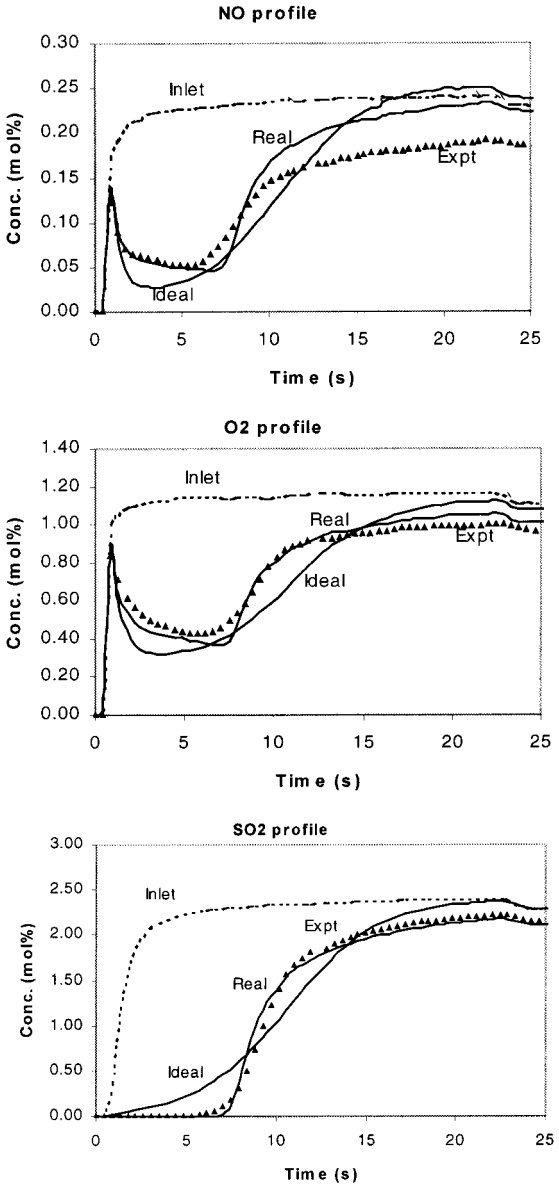

Figure 2. Comparison of simulated and experimental concentrations of NO, O_2, and SO_2 at 387 K and SO_2/NO = 8 without NO_2 (inlet = reactor inlet, expt = measured reactor outlet response, ideal = simulation with uniform surface, real = simulation with nonuniform surface). The markers represent the experiments. The solid lines represent the model calculations obtained by the integration of eqs 1 and 2 with production rates given by eqs 8 and 9 and parameter values given in Table 3.

In Figure 2, the NO and O_2 responses are quite similar in many respects. For example, both NO and O_2 show breakthrough immediately after the step input, in contrast to the SO_2 response. This indicates that neither NO nor O_2 adsorbs on the sites that are available for the adsorption of SO_2. Furthermore, after the initial breakthrough, both the NO and O_2 responses drop quite sharply and pass through minima, before increasing in a way and at a time similar to those of SO_2. The above observations indicate that both NO and O_2 are adsorbed through an intermediate species that could be adsorbed SO_2*. This is corroborated by the observation that SO_2 can independently adsorb on the site, whereas NO and O_2 either alone or together do not adsorb until SO_2 is present either in the gas phase or as an adsorbed species on the solid phase (De Wilde and Marin, 2000).

SO_2 Adsorption. The reaction mechanism proposed to model the experimental results is summarized in Table 2. SO_2 is adsorbed on the active sites primarily involving O^{2-} ions in the form of both Na_2O and γ-Al_2O_3. However, OH^- ions are also present in the sorbent to some extent. The formation of hydroxyl ions is enhanced in the presence of water in the system. Adsorption of SO_2 on O^{2-} and OH^- ions results in corresponding sulfite and bisulfite salts of Na and Al. In Table 2, * represents both O^{2-} and OH^- ions in the sorbent. It can be noted that, in the present work, water is not fed with inlet gas. Even then, some water is released from the sorbent to the outlet gas as reported by De Wilde and Marin (2000). This may be due to the interaction of hydroxyl ions with bisulfate of Na/Al. The latter is formed after SO_2 is adsorbed on the hydroxyl ions. Nevertheless, the presence of water in the inlet gas enhances the concentration of OH^- in the sorbent. This leads to an increase in the site capacity of the sorbent. However, this effect can not be observed in the present study, as water was not included in the inlet gas.

Reaction step S1, i.e., the adsorption of SO_2 takes place independently of the presence of other components or surface species. The adsorption of SO_2 on γ-Al_2O_3 and Na/γ-Al_2O_3 has been studied earlier by many researchers (Saad et al., 1995; Mitchell, 1996). For example, Saad et al. (1995) reported the positive effect of Na on the SO_2 adsorption onto γ-Al_2O_3 and concluded that the Al−O−Na group is primarily responsible for the chemisorption of SO_2. As reported by Zotin and Faro (1989), the presence of Na increases the SO_2 adsorption capacity from 1.5 mol/nm^2 to 2.6 mol/nm^2 at 373 K. Mitchell et al. (1996) reported that, at low Na loading up to 1 wt %, Na acts as a promoter for the formation of an adsorbed sulfite or sulfate that has a structure similar to that of aluminum sulfite or sulfate. However, at high Na loading, a second type of sulfite/sulfate similar to sodium sulfite/sulfate forms, which is more stable than the former type and, therefore, more difficult to regenerate. Further, it is also reported that sulfites could be oxidized to sulfates even without the presence of gas-phase oxygen. Reaction step S1 in Table 2 stands for all of the SO_2 molecules adsorbed on the sorbent surface either by sodium or by aluminum oxide. The adsorbed SO_2 primarily remains as sodium and aluminum sulfites at the begining which are subsequently oxidized to the corresponding sulfate forms.

NO_2 Adsorption. Reaction step S2 indicates direct adsorption of NO_2 onto the sorbent surface. This is quite expected as NO_2 can adsorb on the O^{2-} or OH^- ions of Al and Na to form corresponding nitrite/nitrate or binitrite/binitrate. Indeed, as reported by Szanyi and Paffett (1996), NO_2 adsorbs on the sodium oxide sites to form sodium nitrite/nitrate. Similar observations were also made in the study of NO_2 adsorption over barium aluminate sorbent with or without Pt impregnation (Hodjati et al., 1998).

NO and O_2 do not adsorb on the sorbent independently or together (De Wilde and Marin, 2000). This indicates that the following reactions do *not* occur on the surface as such:

$$\mathrm{NO} + * \not\rightarrow \mathrm{NO}^* \qquad \text{(A)}$$

$$^1/_2\,\mathrm{O_2} + * \not\rightarrow \mathrm{O}^* \qquad \text{(B)}$$

In fact, O_2 does not adsorb on the surface even in the presence of SO_2 if NO is not present. Therefore, the

Table 2. Reaction Steps/Paths Considered in the Kinetic Modeling of SO_2/NO_x Adsorption on Na/γ-Al_2O_3

reaction step/path	elementary reaction steps/ lumped reaction path	active sites covered per mole of surface species
S1	$SO_2 + * \xrightarrow{k_1} SO_2*$	1
S2	$NO_2 + * \xrightarrow{k_2} NO_2*$	1
S3	$SO_2* + * \xrightarrow{k_3} SO_2**$	2
S4	$NO + O_2 + SO_2** \xrightarrow{k_4} [(NO_2)(SO_3)]* + *$	1
P1	$[(NO_2)(SO_3)]* + \{9SO_2*, 3O_2\} \xrightarrow{k_5} R_t10*$	10
P2	$R_t10* + O_2 + \{0.5O_2\} \xrightarrow{k_6} R_s10*$	10
P3	$NO_2* + SO_2 + \{2SO_2\} \xrightarrow{k_7} NO + [O(SO_2)_3]*$	1
P4	$NO_2 + R_t10* \xrightarrow{k_8} 2NO + 4O_2 + Q10*$	10

following step is *not* expected to take place either:

$$^1/_2O_2 + SO_2* - \times \rightarrow SO_3* \qquad (C)$$

However, from experiments done with a mixture of NO_2, NO, and O_2, it was observed that NO_2 adsorbed on the surface is partly converted to NO by the following reaction:

$$NO_2* \rightarrow NO + O* \qquad (D)$$

In the above reaction, although NO desorbs to the gas phase, O* still remains on the site itself, as no change is observed in the O_2 concentration in the gas phase. This indicates that the following reaction is *not* likely to take place as such:

$$2O* - \times \rightarrow O_2 + 2* \qquad (E)$$

It was observed earlier (De Wilde and Marin, 2000) that the presence of NO_2 in the gas phase enhances the SO_2 sorption capacity by more than 70% as compared to the experiments done without NO_2, even at lower SO_2 inlet concentration. Per mole of NO_2, 1 mol of NO and no O_2 are released into the gas phase, and 3 mol of SO_2 are adsorbed onto the surface. This is possible because the O* formed in step D can indeed act as a site for the adsorption of the gas-phase SO_2 as follows:

$$3SO_2 + O* \rightarrow [\,O(SO_2)_3]* \qquad (F)$$

The above step is analogous to the adsorption of SO_2 on O^{2-} sites formed with Al as Al−O−SO_2 and sulfite or disulfite of Na, i.e., $Na_2S_2O_5$, which was also observed in the IR spectra by Saad et al. (1995).

Combining steps D and F

$$3SO_2 + NO_2* \rightarrow NO + [\,O(SO_2)_3]* \qquad (G)$$

Step G corresponds to the reaction path P3 in Table 2, which allows for an understanding of the formation of NO during the adsorption of NO_2.

Simultaneous SO_2, NO, and O_2 Adsorption. As explained in steps A and B, NO and O_2 do not adsorb on the sorbent surface as such. It was also indicated that both of these components require an intermediate species for adsorption, which are only formed during the adsorption process. Further, it was observed that the amounts of NO and O_2 adsorbed are strong functions of the amount of SO_2 adsorbed. From the above, it is logical to postulate that the intermediate species could be SO_2*. Moreover, experimentally, it was also found that the final breakthrough of NO and O_2 coincide with the SO_2 breakthrough, suggesting that the adsorptions of NO and O_2 depend on the availability of free sites. It can be noted that the breakthrough of SO_2 occurs because of the nonavailability of free sites. The latter might be responsible for lending its O^{2-} or OH^- ions, albeit temporarily, to an adsorbed SO_2* while forming a sulfate/bisulfate species SO_2** and thereby creating a site with surplus positive ions, similar to those reported in the study of NO adsorption in Cu−ZSM-5 (Centi and Perathoner, 1995). With free sites available and with dioxygen present, the adsorbed NO quickly converts to NO_2 but still remains strongly adsorbed on the surface. Therefore, the presence of both SO_2* and a free site is essential to the formation of the intermediate species SO_2** via step S3, which allows for the NO/O_2 adsorption. It can be noted here that this is the most important and rate-controlling step as far as simultaneous NO/O_2 adsorption is concerned.

Once the SO_2** species is formed, the NO and O_2 react simultaneously with SO_2** via an Eley−Rideal step as shown in reaction step S4. Interestingly, if only NO or O_2 is considered in this step, the resultant model is found to be incapable of simulating the experimental data, indicating that both NO and O_2 are adsorbed simultaneously. Furthermore, formation of such a species is logical from the fact that, during the regeneration of the sorbent, only NO_2 is released and not NO. Szanyi and Paffett (1996) also reported formation of N_xO_y complexes with free Brönsted sites while working on NO/O_2 adsorption in Cu−ZSM-5. It can be noted that, although a free site is required to initiate step S3, regeneration occurs in step S4, thereby keeping the fraction of free sites unaffected. This mechanism is justified by the observation that the SO_2 sorption capacity (which directly depends on free sites) is practically not affected by the NO/O_2 adsorption. The other finding is that step S4 is indeed much faster than step S3. Attempts to reduce the values of the kinetic constants of step S4 result in a poor simulation of the observations, as the model is unable to simulate the very fast drop and sharp rise in the NO/O_2 responses as observed in the experimental data, viz. Figure 2.

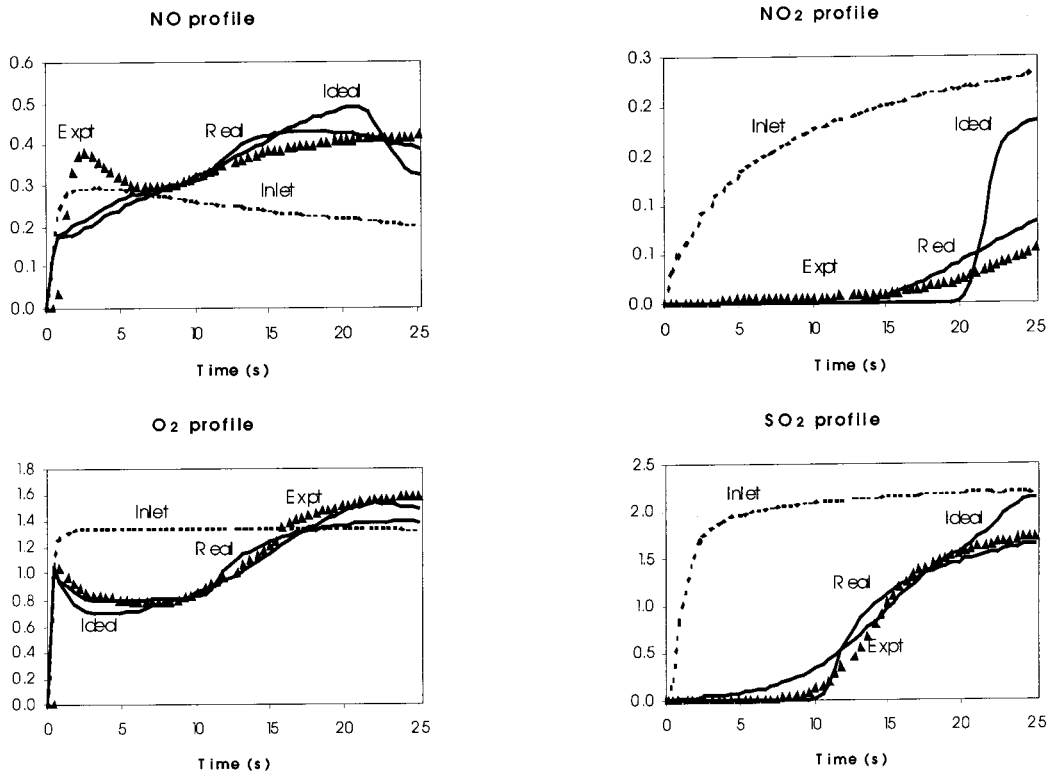

Figure 3. Comparison of simulated and experimental concentrations of NO, O_2, NO_2 and SO_2 at 387 K and $SO_2/NO = 6$ with NO_2 (inlet = reactor inlet, expt = measured reactor outlet response, ideal = simulation with uniform surface, real = simulation with nonuniform surface). The markers represent the experiments. The solid lines represent the model calculations obtained by the integration of eqs 1 and 2 with production rates given by eqs 8 and 9 and parameter values given in Table 3.

The intermediate species $[(NO_2)(SO_3)]^*$ is not fully stable. As in step G with NO_2^*, this species reacts with SO_2^* and gas-phase O_2 in multiple consecutive steps to form a complex. Indeed, such a process can occur even in the absence of NO but with O_2 in the gas phase and at a relatively higher temperature of 423−573 K, as reported by Mitchell et al. (1996). However, in the presence of NO (which is adsorbed as $[(NO_2)(SO_3)]^*$), it appears that sulfate formation is enhanced kinetically, thereby allowing it to take place even at 367−407 K. From the detailed modeling calculations, it was concluded that the complex consists of about 10 mol of SO_2^* and 4 mol of O_2 per 1 mol of NO and that the species could be in the form of $[(NO_2)(SO_x)_{10}]10^*$, abbreviated as R_t10^* to indicate that part of the SO_2^* is also in sulfite form and 10 active sites are covered when this complex is formed. The corresponding reaction for the complex formation is shown as path P1 in Table 2.

Obviously, reaction path P1 consists of several consecutive elementary steps in which each SO_2^* is first attached to the species $[(NO_2)(SO_3)]^*$ and subsequently oxidized to sulfate form in the presence of O_2. However, for the sake of simplicity, these steps have been lumped into one reaction path. It can be noted here that rapid adsorption of O_2 and complex formation toward nitrites/nitrates has also been reported by Szanyi and Paffett (1996) in their study of the adsorption of NO in Cu−ZSM-5 using in situ FTIR at 300 K.

Reaction path P2 indicates complete oxidation of the remaining sulfites into sulfates, which is reported to be relatively slower (Mitchell et al., 1996). However, in the studies of Mitchell et al. (1996), this step was found to occur at 423−573 K, whereas, presently, it occurs even at 373−403 K. This could be due to the presence of NO. Interestingly, it was observed that, with a reduced temperature and a lower SO_2/O_2 ratio, this step essentially slows further. In path P2, R_s10^* indicates a fully oxidized complex in sulfate form with 10 active sites covered. With regard to the O_2 requirement in path P2, the stoichoimetric requirement of O_2 for complete oxidation is 5.5 mol, i.e., 0.5 mol for converting NO to NO_2 and 5 mol for converting 10 mol of SO_2^* species, i.e., sodium or aluminum sulfites, to corresponding sulfates. Because R_t10^* already contains 4 mol of O_2, the balance of 1.5 mol is shown in path P2.

Simultaneous Adsorption of NO, O_2, and SO_2 in the Presence of NO_2. Reaction path P3 is related to the adsorption behavior of the NO_2^* as explained previously viz. Step G. This consists of several elementary steps e.g. a combination of the steps D and F resulting into path P3. It can be noted that the elementary information regarding the presence of O* is lost by such combination. However, this is justified by the fact that step F is potentially much faster than step D, as observed by De Wilde and Marin (2000) in an experiment with a sorbent presaturated with NO_2.

Reaction path P4 is linked with the effect of the gas-phase NO_2 on the complex R_t10^*. This implies that the presence of NO_2 in the gas phase decomposes the complex into gas-phase NO and O_2 and a species Q10*. This will be clear if one follows the experimental results of the simultaneous adsorption of NO, O_2 and SO_2 in the presence of NO_2, as shown in Figure 3. The concentration of NO immediately increases as a result of the release of NO by adsorbed NO_2^* via path P3. However, NO adsorption begins immediately after that as it requires for the formation of sufficient SO_2^* via step S1 (which is relatively much slower than NO_2^* formation via step S2). As expected, simultaneous adsorption of NO and O_2 proceeds via steps S3 until

path P2. However, near the end of the run and coinciding with the NO_2 breakthrough (>15 s), it is observed that the concentrations of both NO and O_2 are sharply increasing. Particularly, the O_2 response is even higher than at the inlet (>17 s), which is only observed if NO_2 is present in the gas phase. This relation with the breakthrough of NO_2 indicates the decomposition of the complex, as shown in path P4.

5. Rate Equations

The production rates of the gas-phase NO, O_2, NO_2, and SO_2 that should be substituted in eq 1 can be written as

$$R_{NO} = -k_4 C_{NO} C_{O2}\, \theta_3 + k_7 \theta_2 C_{SO2} + 2k_8 C_{NO2} \theta_5$$

$$R_{O2} = -k_4 C_{NO} C_{O2}\, \theta_3 - 3k_5 \theta_4 - {}^3/_2 k_6 \theta_5 C_{O2} + 4k_8 C_{NO2} \theta_5$$

$$R_{NO2} = -k_2 C_{NO2} \theta_n - k_8 C_{NO2} \theta_5$$

$$R_{SO2} = -k_1 C_{SO2} \theta_n - 3k_7 C_{SO2} \theta_2 \qquad (8)$$

where θ_j indicates the fractional coverage of the surface species j, i.e., the concentration of the latter divided by the site capacity of the sorbent, C_t.

Similarly, the production rates of the surface species are written as follows:

$$R_1 = k_1 C_{SO2} \theta_n - k_3 \theta_1 \theta_n - 9k_5 \theta_4$$

$$R_2 = k_2 C_{NO2} \theta_n - k_7 C_{SO2} \theta_2$$

$$R_3 = k_3 \theta_1 \theta_n - k_4 C_{NO} C_{O2} \theta_3$$

$$R_4 = k_4 C_{NO} C_{O2} \theta_3 - k_5 \theta_4$$

$$R_5 = k_5 \theta_4 - k_8 C_{NO2} \theta_5 - k_6 C_{O2} \theta_5$$

$$R_6 = k_6 C_{O2} \theta_5$$

$$R_7 = k_7 C_{SO2} \theta_2$$

$$R_8 = k_8 C_{NO2} \theta_5 \qquad (9)$$

Here, R_1−R_8 are the production rates and θ_1–θ_8 are the fractional coverages of the SO_2*, NO_2*, SO_2**, [(NO_2)-(SO_3)]*, R_t10*, R_s10*, [$O(SO_2)_3$]*, and Q10* species, respectively, as shown in Table 2. The second bracket { } in path P1 and P3 (Table 2) indicates that the reaction orders in eqs 8 and 9 are independent of the species or components inside the bracket. The value of θ_n used in the above equations is related to the fraction of free sites on the sorbent. Calculation of this factor depends on the surface model and will be explained next.

The fractional cumulative site coverage θ_c (dimensionless) at any time t is given by

$$\theta_c = \sum_j \beta_j \theta_j \qquad (10)$$

where θ_j is the fractional coverage of the species j and β_j indicates the number of active sites covered per mole of surface species j (as shown in the last column of Table 2). The fractional cumulative site coverage θ_c is defined as the amount of covered sites divided by the site capacity of the sorbent.

The fraction of free sites at any time t is given by

$$\theta_f = 1 - \theta_c \qquad (11)$$

In the Langmuir ideal surface model, the adsorption rate is proportional to the concentration of free sites. This is based on the assumption that the solid surface is homogeneous, i.e., the surface is energetically uniform, and different surface species do not interact with each other. These assumptions usually hold when the fractional coverages of the surface species vary over a limited range. In the present application, however, the coverage varies from zero to complete saturation. Surface models that address the surface inhomogeneity and interaction among species can then be necessary (Boudart and Djéga-Mariadassou, 1984; Temkin, 1967).

One common assumption in the model accounting for nonideality is that the adsorption activation energy (and hence the heats of adsorption) is a linear function of the site coverage

$$E_{ads} = E^\circ_{ads} + \gamma \theta_c \qquad (12)$$

where θ_c is the fractional cumulative site coverage and γ is the factor for the activation energy variation with site coverage.

The physical basis of the above assumption is attributed to the surface heterogeneity, adsorbed species interactions, or a combination of both (Carberry, 1976). For the rate of adsorption, assuming a continuum of ideal patches, integrating against θ_c for $1 \rightarrow 0$, and simplifying for the situation with higher degree of surface nonideality, i.e., $g = (\gamma/RT) \gg 1$, eq 12 leads to

$$r_{ads} = k_{ads} C \exp(-g\theta_c) \qquad (13)$$

Equation 13 is the Elovich real surface model in which the free surface factor θ_f in the ideal surface Langmuir model is now replaced by $e^{-g\theta_c}$, referred to as the Elovich factor.

Therefore, in the rate equations, if the ideal surface Langmuir model is used, $\theta_n = \theta_f = 1 - \theta_c$ of eq 11. However, if the real surface Elovich model is used, $\theta_n = \exp(-g\theta_c)$ as shown in eq 13. It can be noted that in the rate expressions of eqs 8 and 9, the Elovich factor is considered only for the adsorption steps (S1, S2, and S3) and not for the reactions involving surface species. This assumption is justified because the concentrations of the surface species in step S4 and path P1 to P4 are relatively smaller, so that the corresponding activation energies can be assumed independent of the surface coverage of the involved species. The concentrations of SO_2** and [$(NO_2)(SO_3)$]* are smaller (<0.01) because step S4 and path P1 are very fast, as explained later in section 6. The fractional coverages (θ_j) of the R_t10*, R_s-10*, and Q10* species are also relatively smaller (<0.1) as compared to the fraction of free sites θ_f (0→ 1), as several sites are involved for each mole of these species.

In eqs 10 and 11, θ_c indicates the fraction of active sites consumed in the reaction at any time t and is expressed as (viz. the last column of Table 2)

$$\theta_c = \theta_1 + \theta_2 + 2\,\theta_3 + \theta_4 + 10\theta_5 + 10\theta_6 + \theta_7 + 10\theta_8 \qquad (14)$$

6. Parameter Estimates

The estimated values of the kinetic parameters are summarized in Table 3. It is seen that the rate coef-

Table 3. Estimates of the Kinetic Parameters and Site Capacity of the Sorbent for Simultaneous SO_2-NO_x Adsorption on Na/γ-Al_2O_3

parameter	ideal surface model		real surface model	
C_t	0.66[a]		0.93[a]	
g	−		8.00	
step/path	$k_{i,o}$[h]	E_i[f]	$k_{i,o}$[h]	E_i[f]
S1	0.45[b]	4.30	4.22[b]	5.73
S2	31.94[b]	2.32	35.25[b]	2.32
S3	2.19[c]	6.95	2.63[c]	7.79
S4	1835.0[d]	1.26	2052.0[d]	1.26
P1	2174.0[c]	2.58	1971.0[c]	2.58
P2	0.051[b]	35.81	0.049[b]	35.81
P3	0.83[b]	46.34	0.79[b]	46.34
P4	0.79[b]	37.92	0.81[b]	37.92

[a] $mol_{site}\ kg_{sorbent}^{-1}$. [b] $m^3\ mol_{site}^{-1}\ s^{-1}$. [c] $m^3\ mol_{site}^{-1}\ s^{-1}$. [d] $m^6\ mol^{-1}\ mol_{site}^{-1}\ s^{-1}$. [f] kJ mol^{-1}. [h] At 387 K.

ficient for NO_2 adsorption in step S2 is about 10 times greater than that for SO_2 in step S1. Step S3, which is the rate-controlling step for complex formation with NO, is even slower than the SO_2 adsorption rate (step S1). However, the rate coefficients of step S4 and path P1 are much higher than that of step S1, indicating that S4 and P1 are not rate-determining. As discussed earlier, the oxidation of the complex R_t10^* (step P2) occurs very slowly, the corresponding rate coefficient having a value of 0.049 $m^3\ mol_{site}^{-1}\ s^{-1}$. The rate coefficients of paths P3 and P4 are also relatively lower than that of step S1.

The site capacity of the sorbent, C_t is estimated to be 0.66 mol kg^{-1} for the ideal surface model and 0.93 mol kg^{-1} for the real surface model (Table 3). The site capacity C_t could be measured by either SO_2 or NO_2 chemisorption as these components can independently adsorb on the surface. The SO_2 sorption capacity is reported to be 2.8 molecule nm^{-2} at 300 K (Saad et al., 1995) and 2.6 molecule nm^{-2} at 373 K (Zotin and Faro, 1985) for Na/γ-Al_2O_3 sorbent, values that are equivalent to about 0.5 mol kg^{-1} of sorbent capacity. Hence, the estimated C_t values in the present work are reasonable.

The activation energies for SO_2 adsorption (step S1) are 4.30 and 5.73 kJ mol^{-1} for the ideal and real surface models, respectively. These values are much lower than the corresponding value of 21.0 kJ mol^{-1} reported by Andrieu and Smith (1981) for activated carbon. This could be due to the higher basicity of the present sorbent. Kinetic parameters for the simultaneous adsorption of NO and O_2 with SO_2 are not reported in the literature so far. The lower activation energies of step S4 and path P1 result in the higher values of the corresponding rate coefficients. The kinetic parameters of path P2 imply a slower rate of oxidation of the complex R_t10^*, similar to the observation made by Saad et al. (1995) for the oxidation of sulfites to sulfates with Na/γ-Al_2O_3 sorbent. It is further observed in Table 3 that the kinetic parameters have changed little except for those of the first three steps, i.e., S1−S3, when compared for the uniform vs nonuniform surface models. However, this does not mean that the rates of reaction are also similar for the two surface models. As explained in section 5, the value of θ_n in the rate expressions in eqs 8 and 9 depends on the type of surface model considered. For example, in the nonuniform model, $\theta_n = e^{-g\theta_c}$, indicating an exponential variation with site coverage θ_c, whereas for the uniform surface model, θ_n varies linearly with the fraction of free sites $\theta_f = 1 - \theta_c$. Furthermore, in Table 3, it is seen that the preexponential factor $k_{i,o}$ for step S1 is very different for the uniform and nonuniform surface models. Consequently, the latter model simulates the SO_2 response more accurately than the former. Accurate simulation of step S1 is not only important for SO_2 adsorption but also for the simultaneous adsorption of NO and O_2, which occurs in the presence of a species, SO_2**, derived from SO_2* via step S3. For the above reasons, the nonuniform surface model provides a better simulation of the experimental results as seen in Figures 2 and 3.

Figure 4 allows for a comparison of the calculated and measured concentrations of the responses for all the experiments. It is observed that most of the data fall close to the diagonal line, implying satisfactory simulation. However, some deviations are also seen, particularly in the NO response, which corresponds to the same deviation as in Figure 3 for $0 < t < 5$ s. This can be attributed to an artifact in the analysis resulting from the decomposition of NO_2 within the mass spectrometer. Measured values of NO_2 are somewhat lower than the calculated values, possibly because of the limitation of sufficient data for the NO_2 response in the regression. Simulations of the O_2 and SO_2 responses are generally good over a broad range of concentrations, except for some deviations for O_2 at higher concentrations.

7. Uniform vs Nonuniform Surface Model

In Figure 2, it is observed that the nonuniform (real) surface model is able to simulate the results much better than the ideal surface model. For the SO_2 response, the breakthrough of SO_2 occurs almost from the beginning when the ideal surface model is used. This is in contrast to the experimental finding that there is no breakthrough of SO_2 until 7−10 s of introducing the step input. This is expected because, in the ideal surface model, the adsorption rate is first order with respect to the fraction of free sites θ_f. Interestingly, the real surface model simulates the responses very well. Similarly, in the presence of NO_2, Figure 3 illustrates that the real surface model simulates all of the responses better than the ideal surface model. For example, the NO_2 response was largely overestimated by the ideal surface model resulting in a biased NO response after $t > 20$ s, as significant NO is released from the decomposition of the complex R_t10^* via path P4 in the presence of gas-phase NO_2.

The above observations are also evident from the proposed reaction mechanism summarized in Table 2. It is seen that different species interact among one another quite significantly. In fact, the enhancement of SO_2 adsorption by NO_2* and the complex formation of NO with much SO_2* and O_2 suggest that the degree of interaction among various surface species is quite significant. Moreover, in the present application, the fractional cumulative coverage θ_c varies over a broad range, i.e., from zero to complete saturation. Hence, the activation energies for adsorption steps cannot be assumed to be independent of surface coverage. In addition, it can also be argued that the presence of Na at a high loading (5 wt %) in the sorbent, produces at least two types of sulfates one on Na and another on Al, as reported by Mitchell et al. (1996). As the species formed on both types of sites are similar, a dual-site mechanism was not considered. However, the rate of adsorption depends on the type of site, resulting in an intrinsic

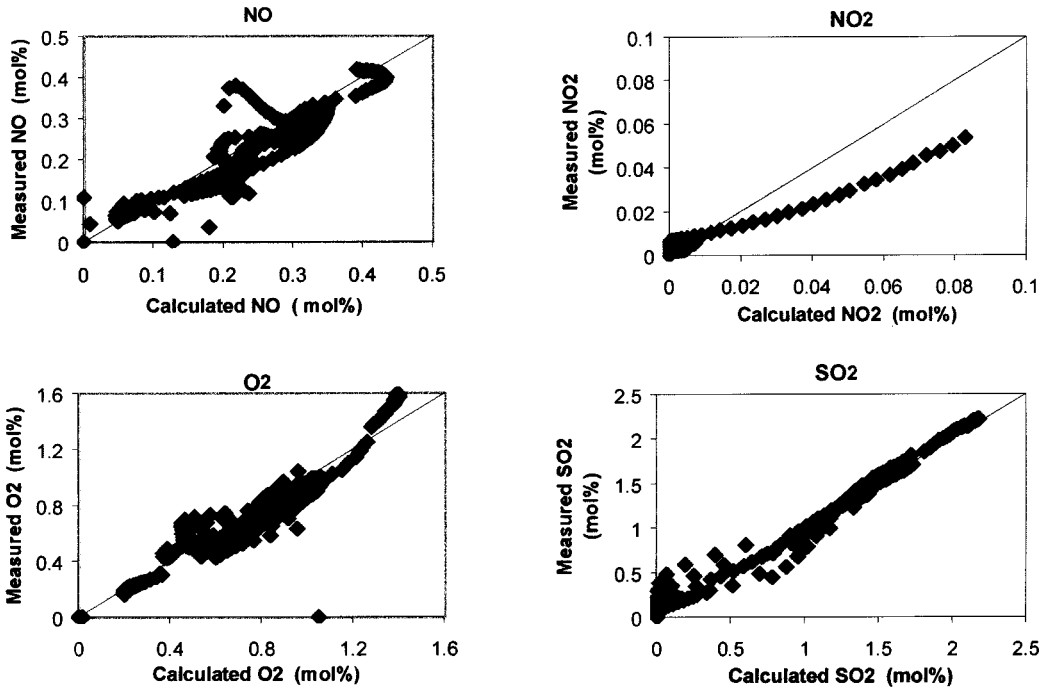

Figure 4. Parity diagrams of the responses for all the experiments at conditions given in Table 1. The calculated values are obtained by the integration of eqs 1 and 2 with production rates given by eqs 8 and 9 and parameter values given in Table 3.

surface nonuniformity. Hence, the real surface model simulates the responses better than the ideal surface model.

8. Main Features of the Proposed Model

In the proposed reaction mechanism (Table 2), both steps S1 and S2 were considered irreversible. The desorption of SO_2* is reported to be prominent above 563 K, i.e., at higher temperature than those investigated in the present work (Saad et al., 1995). Furthermore, the chemisorbed SO_2*, in association with NO and O_2, forms complexes R_t10* and R_s10*. These complexes are so stable that they not only require higher temperature but also strong reducing agents e.g. H_2, CO etc. to desorb. The adsorption of NO_2, on the other hand, was found to be quite fast (Table 3), and no NO_2 desorption was experimentally observed at this temperature. Hence, steps S1 and S2 are considered irreversible in the present application.

For the NO/O_2 adsorption (step S4), it is necessary to have sufficient SO_2**, which can only form if sufficient SO_2* is produced (step S1). Because steps S1 and S3 are rather slow, it takes some time to start the process of SO_2** formation. This results in the initial breakthrough of NO/O_2. However, once the SO_2** is formed, complex formation occurs very rapidly and almost instantaneously, as seen in the very high values of the rate coefficients for step S4 and path P1. Initially, it was assumed that step S3 is reversible. However, because the rate coefficients of the steps following SO_2** formation (S4 and P1) were found to be about one thousand times higher than that of step S3, the latter is irreversible for all practical purposes.

Another feature of the proposed mechanism is the necessity of a free site * in step S3. If the free site is not considered, there is a sharp drop in both NO and O_2 in the simulation and the model is unable to properly predict the minima shown in Figures 2 and 3 between $0 < t < 10$ s. Further, the increase of NO and O_2 after the minimum is also found to be abrupt, unlike the observed smooth transition. In fact, the existence of the minimum is due to two opposing factors: the fast adsorption of NO/O_2 by SO_2** and the availability of free sites. The acquired presence of a free site * in step S3 directly affects the rate of step S3 rather than acting only through SO_2* via step S1. In addition, because SO_2* plays the most important role in the NO/O_2 adsorption, it is natural that an accurate simulation of the SO_2 response (e.g., by using the real surface model) is necessary for a good simulation of NO/O_2 response.

For simultaneous adsorption in the presence of NO_2, it was indicated earlier in section 4 that the NO_2* species opens a new reaction path P3 for the adsorption of additional SO_2. In other words, the SO_2 sorption capacity is enhanced in the presence of NO_2*. As seen in Figure 3 for the simultaneous adsorption with NO_2, the model simulates the SO_2 response fairly well. Further, the model has also simulated the NO and O_2 responses quite closely, except for the deviation in the NO response at $0 < t < 5$ s due to an artifact in the gas analysis as explained in section 6. For the same reason, the inlet step response of NO_2 increases somewhat slowly as in Figure 3. It is observed that O_2 increases very sharply ($t > 15$ s), coinciding with the breakthrough of NO_2. This is due to the decomposition of the complex by the gas-phase NO_2 via path P4.

From Figure 3, it appears that in the presence of NO_2, the concentration of NO is mostly higher than the inlet concentration, as initially NO is produced from NO_2 via path P3 and then by decompostion of the complex R_t-10* via path P4. Therefore, for industrial applications, if the simultaneous adsorption of NO and O_2 is to be achieved, it is very important that NO_2 not be allowed to break through, by ensuring the availability of sufficient free sites for complete adsorption of NO_2 via S2. However, one advantage is that NO_2 adsorbs on the sorbent surface very rapidly, and it also appreciably enhances the SO_2 adsorption capacity.

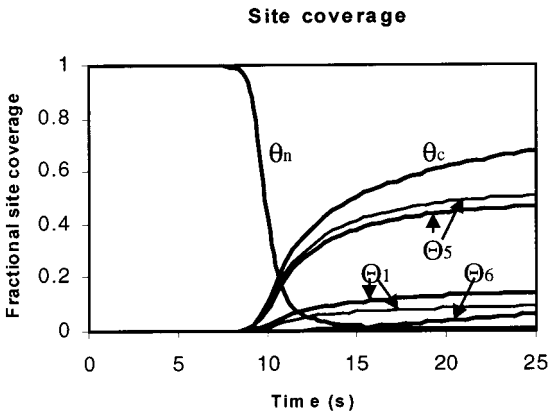

Figure 5. Fractional site coverage of different surface species with varying stoichiometric number β of SO_2* in the complex at 367 K and SO_2/NO = 4 without NO_2 (—, β = 10; ▬, β = 6). $\Theta_j = \beta_j\theta_j$: j = 1, SO_2*; j = 5, R_t10*; j = 6, R_s10*. The fractional cumulative site coverage θ_c is calculated from eq 10 and the Elovich factor θ_n from eq 13. The solid lines represent the calculated values of fractional site coverage $\Theta_j = \beta_j\theta_j$, where the θ_j values are obtained by the integration of eqs 1 and 2 with the production rates given in eqs 8 and 9 and parameter values in Table 3.

The changes in the fractional site coverages Θ_j (= $\beta_j\theta_j$) pertaining to the three important surface species are shown in Figure 5 at the end of the sorbent bed for the experiment at 367 K without NO_2. The cumulative surface coverage θ_c and free site Elovich factor θ_n are also shown in the same figure. Similar time dependencies are observed at the top layer of the bed, except that, in this case, coverages begin to increase right from the introduction of the step input. It can be mentioned that the Θ_j values for the other species were found to be negligible at the end of the bed. In Figure 5, the fractional site coverages Θ_j are presented for two different stoichiometric coefficients of SO_2*, i.e., for β = 10 and 6, for the species R_t10*, R_s10*, and Q10*. It is observed that, for a given β, the fraction of sites covered by SO_2* (i.e., Θ_1) increases from the time when SO_2 breakthrough occurs ($t \approx 7$ s). It is natural to expect that the active adsorption zone will gradually shift from the top of the bed toward the bottom as time passes. This is clearly observed in Figure 5, where no species is formed ($\theta_c = 0$) during the first 7 s. Consequently, when SO_2 breakthrough occurs, the availability of free sites, and thus θ_n, drops very sharply, resulting in lower rates of steps S1 and, more importantly, S3, leading to the accumulation of SO_2* on the surface. It can be noted that the rate of step S3 drops despite the higher SO_2* coverage, because of the sharp drop in θ_n. However, such accumulation of SO_2* is preceded by a large increase in Θ_5, i.e., sites covered by R_t10* species, within a very short time, indicating the faster rate of complex formation, as discussed in section 6. As the sorbent is saturated, the formation of the complex, and thus Θ_5, levels off subsequently because of the nonavailability of free sites ($\theta_n \approx 0$). The slower oxidation of R_t10* to R_s10* continues even after saturation of the sorbent as it does not require any free site. This is demonstrated by a slow increase in Θ_6, i.e., sites covered by R_s10* species, until the end of the run.

9. Effect of Reaction Temperature and Stoichiometry of the Complexes

The results of the experimental data for 367 and 407 K are not shown here. However, there are certain observations on the simulation of the experiment at 367 K. The SO_2 response was predicted by the model very accurately using the same set of global parameters as in Table 3. However, the model was unable to predict the minimum values of NO and O_2 (similar to those at $t \approx 5$ s in Figure 2) for this temperature. Interestingly, it was experimentally observed that, at 367 K, the local minima of NO and O_2 responses are even lower than those at 387 and 407 K. The local minima imply the maximum extent to which NO and O_2 could be removed from the flue gas and hence are termed here the "removal efficiency". To summarize, at 367 K, the removal efficiencies of NO and O_2 are higher than those at 387 and 407 K. One possibility for such an observation is that the rate-controlling step S3 might be reversible with relatively higher activation energy of the backward reaction. However, as discussed in the previous section, step S3 is practically irreversible because of the fast reactions S4 and P1 that follow S3. Therefore, the reverse reaction has no real significance, as observed in the simulation also.

Another possible explanation could be that the stoichiometry of the complex R_t10* changes with reaction temperature. To study the above phenomenon further, an attempt was made to vary the stoichiometric coefficient β for SO_2* and O_2 of path P1. Indeed, it was found that, if path P1 consists of 5 SO_2* (i.e., β = 6) and 2.5 O_2 per molecule of [$(NO_2)(SO_3)$]*, then the model is able to predict the higher removal efficiencies of NO and O_2 satisfactorily. This is further illustrated in Figure 5, which shows the variation of the fractional site coverage Θ_j (= $\beta_j\theta_j$) with different stoichiometric coefficients of SO_2* and O_2.

In Figure 5, the site coverage of SO_2* is 0.14 for β = 6 vs 0.09 for β = 10. This confirms that the coverage of SO_2* species on the surface increases when smaller numbers of SO_2* are involved in complex formation. As seen in Figure 5, neither θ_n nor θ_c is affected by changing the stoichiometry of the complex β. This is due to the fact that there is no net consumption of free sites in the formation of the complex in the combined steps of S3 + S4 and path P1. As θ_n is unaffected by β, the rate of step S1 remains the same. Thus, the rates of step S3 and path P1 determine the change in the SO_2* coverage. The rate of step S3 increases with smaller β because of the increased coverage by SO_2* species, as θ_n has not changed. As S3 is the rate-controlling step in the complex formation, this results in a higher rate of step S4 and path P1. However, with a smaller β, path P1 requires proportionately much less SO_2*, which is not compensated for by the increased rate of P1. Therefore, there is a net increase in the SO_2* coverage with decreasing β.

Because the coverage by SO_2* (Θ_1 in Figure 5) is higher at lower β and θ_c is independent of β in the present case, this results in a reduction in the fractional site coverage Θ_5 pertaining to R_t10*. Indeed, in Figure 5, it is seen that Θ_5 is smaller when β is reduced (0.47 for β = 6 vs 0.5 for β = 10). However, when the corresponding species coverages (θ_j) are calculated, θ_5 is higher at lower value of β (0.0783 at β = 6 vs 0.05 at β = 10). Similarly, θ_6 is also higher at lower β, although the fractional site coverage Θ_6 is the same as seen in Figure 5. Obviously, the higher species coverages θ_5 and θ_6 at the lower β of 6 directly correspond to higher removal efficiencies of NO and O_2 , i.e., lower minimum values of concentrations at the outlet. Therefore, for

industrial applications, operation at the relatively lower temperature of 367 K is more attractive for achieving the overall goal of maximum NO and SO_2 removal from the flue gas.

10. Conclusion

A transient kinetic model for the simultaneous adsorption of SO_2/NO_x on $Na/\gamma\text{-}Al_2O_3$ has been developed. It is based on several elementary steps and a few lumped reaction paths. The first two reaction steps correspond to direct adsorption of SO_2 and NO_2 on the sorbent sites. However, NO and O_2 adsorb on the surface only simultaneously and in the presence of SO_2** species. This latter species is formed by the interaction of SO_2* with a free site. The species SO_2** aids in the rapid adsorption of NO and O_2 via an Eley−Rideal step to form $[(NO_2)(SO_3)]$*. The latter is followed by several consecutive steps involving more SO_2* species as well as O_2 leading to the formation of a complex R_t-10*. Complete oxidation of sulfites (R_t10*) to sulfates (R_s10*) occurs in the presence of additional O_2. The enhanced capacity of SO_2 adsorption is explained by the NO_2* species interacting with SO_2 from the gas phase. The presence of NO_2 in the gas phase leads to the decomposition of the complex R_t10*, corresponding to a significant desorption of NO and O_2.

Nonuniformity of the surface is taken into account by describing the steps involving free sites by Elovich rate equations. The model provides insight into the reaction mechanism and allows for a quantification of the importance of the steps involved. The fastest adsorption is that of NO_2, the adsorption of SO_2 being 1 order of magnitude slower. The rate of NO adsorption is potentially even faster than that of NO_2 but depends on the concentrations of O_2 and SO_2**. The latter species results from the relatively slow surface reaction between SO_2* and a free site. In that sense, the surface reaction determines the rate of NO adsorption. However, the stoichiometry of the complex R_t10*, i.e., β, can also significantly change the NO adsorption rate by altering the coverage of SO_2* species in the surface. In addition, the model also corroborates the interesting observation of higher removal efficiencies of NO and O_2 at lower temperatures by considering the variation of the stoichiometry of the complexes with reaction temperature.

Acknowledgment

This work was financed by the European Commission within the framework of the Non-Nuclear Energy Program, Joule III project under contract JOF3-CT95-0012 and Thermie project under contract SF 243/98 DK/BE/UK (project partners: Laboratorium voor Petrochemische Techniek, Universiteit Gent, FLS miljo a/s, Denmark, and Howden Air & Gas Division, U.K.). The Fonds voor Wetenschappelijk Onderzoek (FWO), Vlaanderen, Belgium, is acknowledged for funding of the mass spectrometer.

Nomenclature

Bi_m = mass Biot number = $k_g r/D_e$, dimensionless
C = gas-phase concentration of a component, mol m_{gas}^{-3}
C_i = gas-phase concentration of the component i, mol m_{gas}^{-3}
C_t = site capacity of the sorbent, $mol_{site}\ kg_{sorbent}^{-1}$
$C_i°(t)$ = reactor inlet concentration of the gas-phase component i as a function of time t, mol m_{gas}^{-3}
D_e = effective diffusion coefficient, m^2/s
D_m = molecular diffusivity of the gas, m^2/s
d_p = particle diameter, m
d_r = reactor diameter, m
E_i = activation energy, kJ/mol
k_g = mass transfer coefficient, m/s
$k_{i,o}$ = reparametrized preexponential factor of the step i at an average temperature T_{av}, dimension as in Table 3
L = sorbent bed length, m
n = number of observations, dimensionless
r = particle radius, m
r_o = radius of micropores in the sorbent, m
R = gas constant, (KJ mol^{-1} K^{-1})
Re = Reynolds number = $\rho u_s d_p/\mu$, dimensionless
R_i = net production rate of the component i in the gas phase, mol mol_{site}^{-1} s^{-1}
R_j = net production rate of the species j, mol mol_{site}^{-1} s^{-1}
S = residual sum of squares for all the responses and observations, dimensionless
Sc = Schmidt number = $\mu/\rho D_v$, dimensionless
Sh = Sherwood number = $k_g d_p/D_v$, dimensionless
T_{av} = average reactor temperature of all the experiments, K
T = reactor temperature, K
t = transient time from the introduction of the step/pulse input, s
u_s = gas superficial velocity, m^3_{gas} $m^{-2}_{reactor}$ s^{-1}
$y_{k,i}$ = observed value of the ith response during the kth observation
$\hat{y}_{k,i}$ = calculated value of the ith response during the kth observation.
z = axial length of the reactor, m

Greek Notation

θ_c = fractional cumulative site coverage, dimensionless
θ_j = fractional coverage by the species j, $mol_{species}/mol_{site}$
$\Theta_j = \beta_j\theta_j$ = fractional site coverage by the species j, dimensionless
γ = factor for the activation energy variation with site coverage, J/mol
ρ_s = sorbent particle density, $kg_{sorbent}$ $m^{-3}_{particle}$
ρ = density of the gas, kg m^{-3}
μ = viscosity of the gas, kg m^{-1} s^{-1}
ϵ = effective porosity of the reactor bed = $\epsilon_b + (1 - \epsilon_b)\epsilon_p$, m^3_{gas} $m^{-3}_{reactor}$
ϵ_p = particle porosity, m^3_{gas} $m^{-3}_{particle}$
ϵ_b = void fraction of the reactor bed, m^3_{gas} $m^{-3}_{reactor}$
β_j = number of active sites covered by the surface species j (mol_{site} $mol^{-1}_{species}$)
v = number of independent responses, dimensionless

Literature Cited

Andrieu, J.; Smith, J. M. Adsorption Rates of Sulfur Dioxide and Hydrogen Sulfide in Beds of Activated Carbon. *AIChE J.* **1981**, *27*, 840.

Boudart, M.; Djéga-Mariadassou, G. *Kinetics of Heterogeneous Catalytic Reactions*; Princeton University Press: Princeton, NJ, 1984.

Carberry, J. J. *Chemical & Catalytic Reaction Engineering*; McGraw-Hill Chemical Engineering Series; McGraw-Hill: New York, 1976.

Centi, G.; Perathoner, S. Adsorption and Reactivity of NO on Cu−Al_2O_3 Catalyst. *J. Catal.* **1995**, *152*, 93.

Chihara, K.; Suzuki, M.; Kawazoe, K. Adsorption Rate on Molecular Sieving Carbon by Chromatography. *AIChE J.* **1978**, *24*, 242.

Cho, S. M. Properly Apply Selective Catalytic Reduction for NO_x Removal. *Chem. Eng. Prog.* **1994,** *Jan*, 39.

Dekker: F. H. M.; Bliek, A.; Kapteijn, F.; Moulijn, J. A. Analysis of Mass and Heat Transfer in Transient Experiments over Heterogeneous Catalysts. *Chem. Eng. Sci.* **1995**, *50*, 3573.

Deo, A. V.; Dalla, L. I. G. Infrared Studies of the Adsorption and Surface Reactions of Hydrogen Sulfide and Sulfur Dioxide on Some Aluminas and Zeolites. *J. Catal.* **1971**, *21*, 270.

De Wilde, J.; Marin, G.B. Investigation of Simultaneous Adsorption of SO_2 and NO_x on Na-γ-Al_2O_3 with Transient Techniques. *Catal. Today*, in press.

Himmelblau, D. M. *Applied Nonlinear Programming*; McGraw-Hill: New York, 1972.

Hodjati, S.; Bernhardt, P.; Petit, C.; Pitchon, V.; Kiennemann, A. Removal of NO_x: Part I. Sorption/Desorption Process on Barium Aluminate. *Appl. Catal. B* **1998**, *19*, 209.

Summary on Environmental Processes '98. *Hydrocarbon Process.* **1998**, *Aug*, 71.

Karge, H. G.; Dalla Lana, I. G. Infrared Studies of SO_2 Adsorption on a Claus Catalyst by Selective Poisoning of Sites. *J. Phys. Chem.* **1984**, *88*, 1538.

Ma, W. T.; Chang, M.; Haslbeck, J. L.; Neal, L. G. NOXSO SO_2/NO_x Flue Gas Treatment Process Adsorption Chemistry and Kinetics: Novel Adsorbents and their Enviornmental Applications. *AIChE Symp. Ser.* **1995**; *91*, 309.

Mitchell, M. B.; Sheinker, V. N.; White, M. G. Adsorption and Reaction of Sulfur Di-oxide on Alumina and Sodium Impregnated Alumina. *J. Phys. Chem.* **1996**, *100*, 7550.

Mortensen, L. Experience from a 10 MW Demonstration Project with an Innovative SO_x and NO_x Adsorption Process (SNAP), EPRI−EPA−DOE SO_2 Control Symposium, Miami Beach, FL, 1995.

Nibbelke, R. H.; Nivergeld, A. J. L.; Hoebink, H. B. J.; Marin, G. B. Development of a Transient Kinetic Model for the CO Oxidation by O_2 over a Pt/Rh/CeO_2/γ-Al_2O_3 Three-way Catalyst. *Appl. Catal. B* **1998**, *19*, 245.

FORTRAN Library Manual, Mark 15; Numerical Algorithm Group: Oxford, U.K., 1991.

Saad, M. A. B.; Ivanov, V. A.; Lavalley, J. C.; Nortier, P.; Luck, F. Comparative Study of the Effects of Sodium Impurity and the Amorphisation on the Lewis Acidity of γ-Alumina. *Appl. Catal. A* **1993**, *94*, 71.

Saad, M. A. B.; Saur, O.; Wang, Y.; Tripp, C. P.; Morrow, B. A.; Lavelley, J. C. Effect of Sodium on Adsorption of SO_2 on Alumina and on its Reaction with H_2S. *J. Phys. Chem.* **1995**, *19*, 4620.

Schiesser, W. E. *The Numerical Method of Lines: Integration of Partial Differential Equations*; Academic Press: San Diego, CA, 1991.

Szanyi, J.; Paffett, M. T. The Adsoption of NO in Cu−ZSM-5. *J. Catal.* **1996**, *164*, 232.

Temkin, M. I. Kinetics of Reactions including Adsorption Chemical Equlibria. *Kinetika I Kataliz.* **1967**, *8*, 1005.

van der Linde, S. C.; Nijhuis, T. A.; Dekker: F. H. M.; Kapteijn, F.; Moulijn J. A. Mathematical Treatment of Transient Kinetic Data: Combination of Parameter Estimation with Solving the related Partial Differential Equations. *Appl. Catal. A* **1997**, *151*, 27.

Zotin, J. L.; Faro, A. C., Jr. Influence of the Basicity of the Alumina Catalyst on their Activity in H_2S/SO_2 Reaction. *Appl. Catal.* **1985**, *16*, 49.

Received for review May 31, 2000
Revised manuscript received September 14, 2000
Accepted September 21, 2000

IE000532O